International Journal of Minerals, Metallurgy and Materials
Volume 30, Number 7, July 2023, Page 1329
https://doi.org/10.1007/s12613-023-2597-6

Influence of band microstructure on carbide precipitation behavior and toughness of 1 GPa-grade ultra-heavy gauge low-alloy steel

Peng Han[1,2], *Zhipeng Liu*[1], *Zhenjia Xie*[1,✉], *Hua Wang*[2], *Yaohui Jin*[2], *Xuelin Wang*[1,3], *and Chengjia Shang*[1,3]

1) Collaborative Innovation Center of Steel Technology, University of Science and Technology Beijing, Beijing 100083, China
2) State Key Laboratory of Metal Material for Marine Equipment and Application, Anshan 114000, China
3) Yangjiang Branch, Guangdong Laboratory for Materials Science and Technology (Yangjiang Advanced Alloys Laboratory), Yangjiang 529500, China
(Received: 29 September 2022; revised: 26 December 2022; accepted: 6 January 2023)

Abstract: This study investigated the influence of band microstructure induced by centerline segregation on carbide precipitation behavior and toughness in an 80 mm-thick 1 GPa low-carbon low-alloy steel plate. The quarter-thickness (1/4t) and half-thickness (1/2t) regions of the plate exhibited similar ductility and toughness after quenching. After tempering, the 1/4t region exhibited ~50% and ~25% enhancements in both the total elongation and low-temperature toughness at −40°C, respectively, without a decrease in yield strength, whereas the toughness of the 1/2t region decreased by ~46%. After quenching, both the 1/4t and 1/2t regions exhibited lower bainite and lath martensite concentrations, but only the 1/2t region exhibited microstructure bands. Moreover, the tempered 1/4t region featured uniformly dispersed short rod-like $M_{23}C_6$ carbides, and spherical MC precipitates with diameters of ~20–100 nm and <20 nm, respectively. The uniformly dispersed nanosized $M_{23}C_6$ carbides and MC precipitates contributed to the balance of high strength and high toughness. The band microstructure of the tempered 1/2t region featured a high density of large needle-like M_3C carbides. The length and width of the large M_3C carbides were ~200–500 nm and ~20–50 nm, respectively. Fractography analysis revealed that the high density of large carbides led to delamination cleavage fracture, which significantly deteriorated toughness.

Keywords: band microstructure; carbides; toughness; heavy gauge steel; centerline segregation

1. Introduction

High-strength low-alloy steels have been widely used in ship hulls, bridges, buildings, and offshore structures, owing to their excellent combination of high strength, high toughness, good weldability, and low cost [1]. With the increasing development of large-scale machinery and equipment in the field of marine engineering, there is a strong demand for 1 GPa-strength-grade ultra-heavy gauge steel plates for weight reduction, safety improvement, and low carbon emissions [2–3]. In addition, high toughness at −40°C is urgently desired to meet the requirements of deep-sea resource exploration. However, achieving a homogeneous microstructure over the entire thickness is challenging, resulting in differences in mechanical properties among regions of different thicknesses [4]. Realizing uniform deformation over the whole thickness during controlled rolling processes is difficult. Moreover, the liquid-phase alloying element undergoes segregation at the solidification front, owing to the difference in solubility between the liquid and solid phases, resulting in composition inhomogeneity [5]. This inhomogeneity, resulting from centerline segregation, becomes significant in the center region owing to the slow cooling rate.

Studies have revealed that eliminating the chemical inhomogeneity caused by centerline segregation is difficult, and the inhomogeneity usually results in the formation of a banded microstructure in the segregated region [6–7]. Owing to the high concentration of alloying elements, particularly manganese, hard martensite forms in the banded microstructure, resulting in high internal stress in martensite and deterioration of low-temperature toughness [8]. Although the internal residual stress can be eliminated through further tempering, the carbide precipitation behavior may be different owing to the chemical inhomogeneity, different chemical compositions result in the differences in type, size and density of carbide precipitates. However, to the best of our knowledge, the effects of centerline segregation-induced chemical inhomogeneity on carbide precipitation behavior and the consequent mechanical properties of 1 GPa ultra-heavy gauge low-carbon low-alloy steels have not been systematically studied. The type, size, morphology, distribution, and density of carbide precipitates considerably affect low-temperature toughness [9–10]. Large and brittle particles result in cleavage fracture and deteriorate low-temperature toughness.

✉ Corresponding author: Zhenjia Xie E-mail: zjxie@ustb.edu.cn

The present study comparatively investigated microstructure evolution, carbide precipitation, and their effects on mechanical properties for 1/4t and 1/2t regions of an 80 mm-thick ultra-high-strength low-carbon low-alloy steel produced via quenching and tempering. Transmission electron microscopy (TEM) analysis was conducted to elucidate the influence of centerline segregation on carbide precipitation behavior and toughness. The results elucidate the structure–property relationship in 1 GPa ultra-heavy gauge low-carbon low-alloy steel produced via quenching and tempering.

2. Experimental

The chemical composition of the studied steel was 0.16wt% C, 0.2wt% Si, 0.55wt% Mn, 0.47wt% Cr, 2.0wt% Ni, 0.65wt% Mo, 0.08wt% V, 0.015wt% Ti, and 0.0015wt% B, and the balance was Fe. The steel was melted and continuously cast into a 250 mm-thick slab. Before hot rolling, the slab was homogenized at 1180°C for 2 h. Then, the slab was rough-rolled to 185 mm with a >20% reduction for each pass. The start temperature of the rough rolling stage was 1000°C. Afterward, the slab was finish-rolled to an 80 mm plate at a start temperature of 830°C. Finally, the plate was air-cooled to ambient temperature. The hot-rolled steel plate was reheated to 860°C and held for 2 h and then quenched to ambient temperature. The quenched plate was finally tempered at 640°C for 2 h.

After each step of quenching and tempering, dog bone-shaped round tensile specimens with a gage length of 110 mm and a diameter of 8 mm and V-notched specimens of dimensions 55 mm × 10 mm × 10 mm in the transverse direction were prepared from the 1/4t and 1/2t regions of the studied steel plate. The center lines of the 1/4t and 1/2t regions are schematically shown in Fig. 1. Tensile tests were conducted at an extension rate of 2.5×10^{-3} s^{-1} using an extensometer of 50 mm at room temperature. Charpy impact tests were conducted at −40°C.

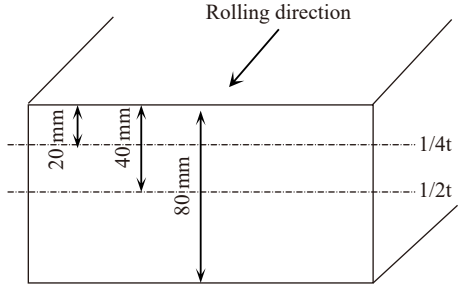

Fig. 1. Schematic showing the center lines for 1/4t and 1/2t regions.

Heat-treated samples with different thickness positions were mechanically polished to mirror finish and etched with 4vol% nital according to standard metallographic procedures for optical microscopy (OM) and scanning electron microscopy (SEM) analyses. SEM was conducted using a TESCAN MIRA 3 LMH field-emission scanning electron microscope operated at 10 kV. Electron backscatter diffraction (EBSD) analysis was conducted on the 1/4t and 1/2t regions of the quenched plate using a TESCAN CLARA GMH field-emission scanning electron microscope equipped with the Oxford Instruments SYMMETRY S2 EBSD detector with a voltage of 20 kV and a step size of 0.1 μm. The EBSD samples were mechanically ground and polished, and finally, electrolytic polishing was conducted using a 10vol% perchloric acid alcohol solution at a current of ~1 A for ~20 s. EBSD data were analyzed using AZtecCrystal software. To study the composition, size, and morphology of carbide precipitates, the carbon extraction replica approach was used for the tempered samples. First, the specimens were polished and etched with 4vol% nital. Then, carbon was evaporated onto the etched surface. Finally, the surface was scored to ~3 mm squares and etched again with 4vol% nital. Subsequently, the extracted replicas were rinsed with distilled water and placed on the copper grid and dried. TEM analysis was conducted using the Thermo Fisher Scientific Talos F20 transmission electron microscope equipped with an energy-dispersive X-ray spectrometer operated at 200 kV.

3. Results

3.1. Mechanical properties

The yield strength, tensile strength, total elongation, and low-temperature toughness of the studied steel plate are summarized in Fig. 2. The 1/4t region of the quenched steel plate exhibited high yield strength and tensile strength: 990 and 1229 MPa, respectively. Owing to the relatively low cooling rate at the 1/2t region, the yield strength and tensile strength were 938 and 1149 MPa, respectively. The 1/4t and 1/2t regions exhibited similar elongations. After tempering, the yield strength of the 1/4t region remained at 999 MPa, while that of the 1/2t region slightly decreased to 909 MPa. The tensile strengths of the 1/4t and 1/2t regions decreased to 1049 and 983 MPa, respectively. The total elongation and low-temperature toughness of the 1/4t region were improved by ~50% and ~25% after tempering, while the toughness of the 1/2t region was significantly decreased by ~46%.

3.2. Microstructure

Fig. 3 presents the OM images of the quenched steel plate at the 1/4t and 1/2t regions. The 1/4t region exhibited a uniform microstructure (Fig. 3(a)), while the 1/2t region exhibited microstructure bands (Fig. 3(b), white arrows). The band length was from ~500 to >1000 μm, and the width was ~50–100 μm. The band microstructure formation was caused by the chemical inhomogeneity in the center region of the cast slab [11]. During casting, carbon and manganese were redistributed in the solid austenite and liquid owing to the difference in solubility between the two phases; consequently, carbon and manganese were enriched in the unsolidified liquid. The alloying enriched liquid transformed to austenite as the segregation region. The segregation regions were elongated into bands, and the enrichment of the alloy elements was

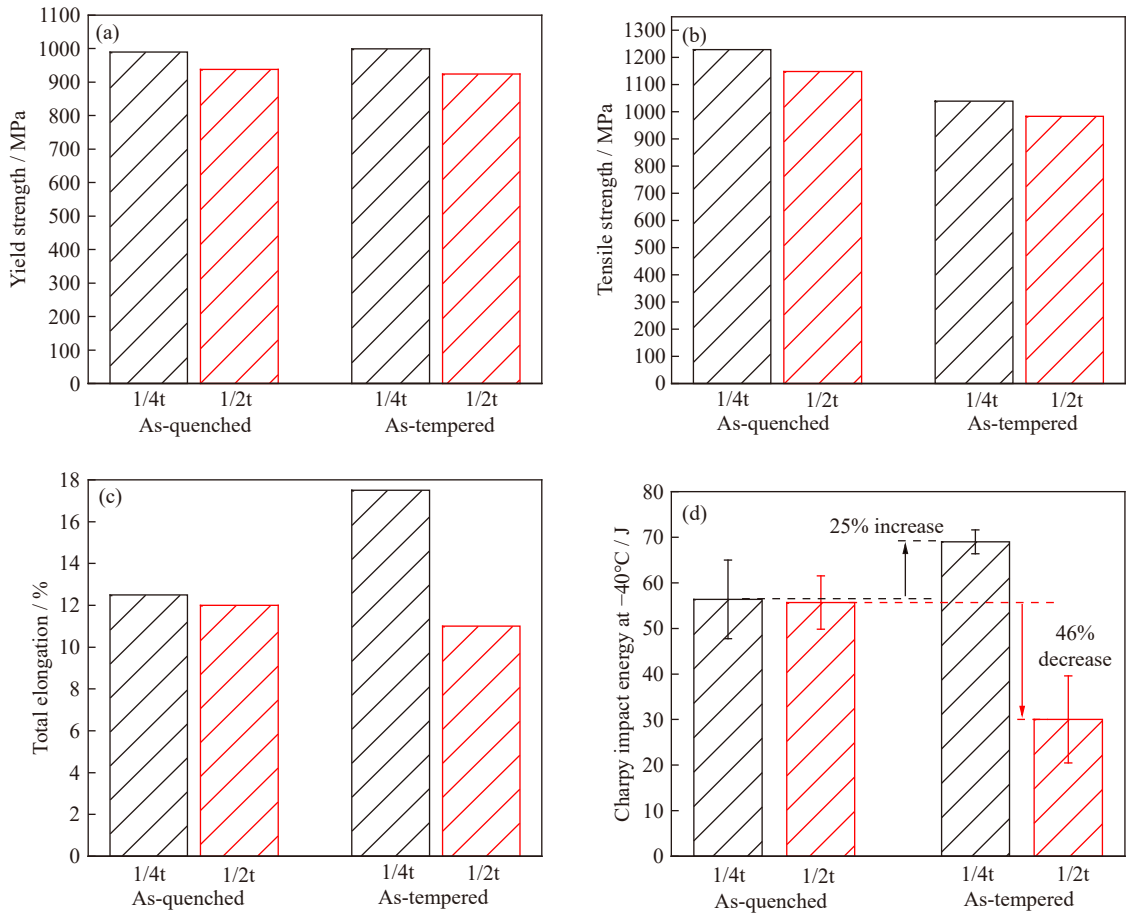

Fig. 2. Mechanical properties for the studied steel plate at different thickness positions after quenching and tempering: (a) yield strength, (b) tensile strength, (c) total elongation, and (d) Charpy impact energy at −40°C.

inherited after controlled rolling. Although a low-manganese alloy was designed in this study, manganese segregation occurred with carbon segregation. Manganese can hardly be homogenized during hot working and reaustenitization owing to its low diffusion coefficient. Moreover, manganese reduced the carbon activity in austenite. A higher carbon content in the manganese-segregated austenite was needed to maintain the chemical potential balance [12–13]. Therefore, carbon can also hardly undergo homogenization. According to early studies [14–15], higher carbon content resulted in a lower corrosion rate during etching. Therefore, the microstructure bands were segregated with carbon, resulting in a relatively low etching rate, and finally, white bands were detected via OM. The high-magnification images revealed that no significant difference occurred between 1/4t and 1/2t (Fig. 3(c) and (d)). The microstructures of both regions were composed of dark fine and bright coarse laths.

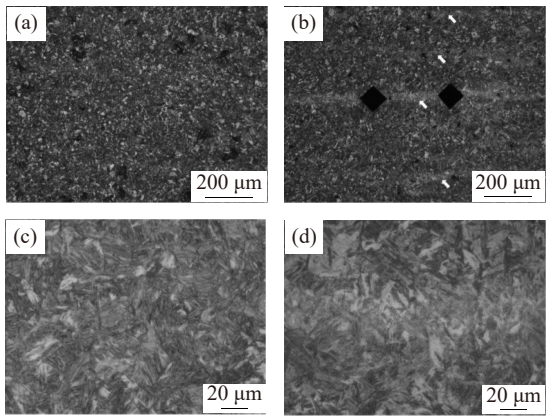

Fig. 3. Optical micrographs for 1/4t (a, c) and 1/2t (b, d) regions of the quenched steel plate.

Fig. 4(a) shows the SEM microstructure of the quenched steel plate at the 1/4t region. To characterize the microstructure in the band, hardness indentations were made in the microstructure band (Fig. 3(c) and (d)). The corresponding SEM image of the banded microstructure is given in Fig. 4(b). The 1/4t region and the 1/2t band region showed no significant difference in the microstructure. The SEM images confirmed that the quenched steel plate contained coarse

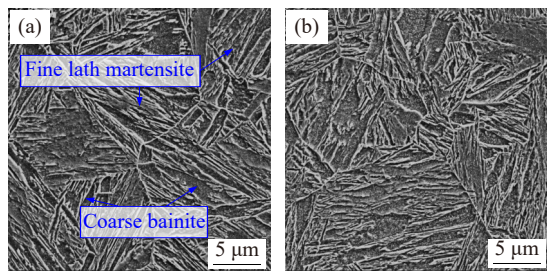

Fig. 4. SEM micrographs for different regions of the quenched steel plate: (a) the 1/4t region and (b) the banded microstructure in the 1/2t region in Fig. 3(d).

bainite and fine martensite laths. The coarse lath bainite featured a width of ~1–2 μm. In addition, the coarse lath microstructure featured fine carbides (Fig. 4(a)). The formation mechanism of coarse bainite laths has been proposed by Bhadeshia and co-authors [16–17]. The researcher reported that when bainite sheaves in the same crystallographic orientation as parallel habit planes form at temperatures near the martensite-start temperature, and there is sufficient driving force to overcome the strain energy associated with the coarser plate, coalesced bainite forms through the merging of the adjacent sheaves with identical orientation to form a single large plate. The supersaturated carbon precipitates as carbides. With further cooling, the untransformed austenite is transformed into fine lath martensite, in which no carbide occurs, as shown in Fig. 4(a).

Fig. 5 presents the SEM microstructure of the tempered steel plate. The 1/4t sample contained fine and uniformly dispersed carbides (Fig. 5(a)). The carbides were mainly spherical within tempered laths. A few rod-like carbides occurred along the grain boundaries and lath boundaries. The tempered 1/2t sample also featured microstructure bands (Fig. 5(b), white bands). The microstructure of the white bands contained a high density of large carbides (Fig. 5(c)). In contrast, the carbides outside the banded microstructure were as fine and uniform as those of the 1/4t region. The high density of large carbides formed in the banded microstructure may be detrimental to the ductility and low-temperature toughness of the tempered 1/2t sample.

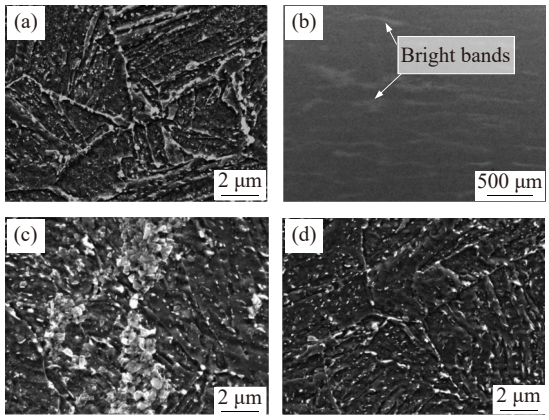

Fig. 5. SEM micrographs for different regions of the quenched and tempered steel plate: (a) 1/4t region and (b) 1/2t region; (c) and (d) are the high-magnification images for the bright-band microstructure and dark matrix in (b), respectively.

3.3. Characterization of carbide precipitation

Detailed TEM analysis was conducted to elucidate the influence of the segregated band microstructure on carbide precipitation behavior. The obtained TEM bright-field images are presented in Fig. 6. To observe the carbide distribution after tempering, numerous photos were used to clarify the TEM panorama under a grid field of view (Fig. 6(a) and (c)). The 1/4t sample featured a fairly homogenous carbide distribution (Fig. 6(a)), while the 1/2t sample exhibited a heterogenous distribution (Fig. 6(c)). In the 1/4t sample, the carbides were mainly spherical and short-rod-like; only a few needle-like carbides existed (Fig. 6(b)). The spherical carbides were nano-size, and their diameter ranged from several nanometers to ~100 nm, while the needle-like carbides were ~1 μm in length and ~50 nm in width. The 1/2t sample featured a heavy-precipitation region (Fig. 6(c)). In this region, the carbides were mainly needle-like and coarse-rod-like (Fig. 6(d)). The needle-like carbides were ~1 μm in length and ~50–100 nm in width, similar to the 1/4t sample. Numerous coarse rod-like carbides aggregated into a dense precipitate group. The coarse rod-like carbides were mainly ~100–200 nm on the long axis and ~50–100 nm on the short axis. Few spherical nanosized carbides occurred in the precipitate group.

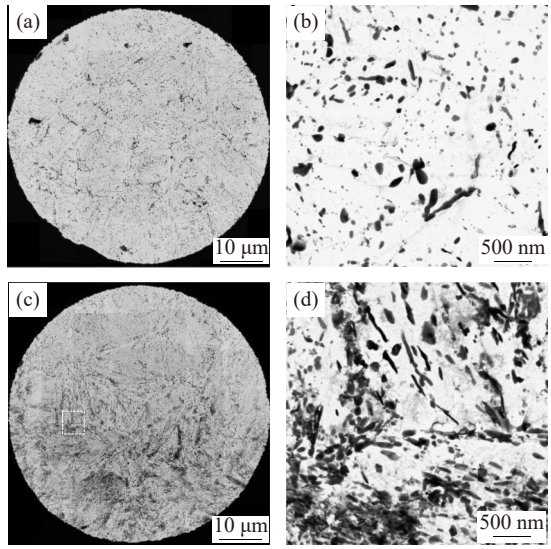

Fig. 6. TEM micrographs showing carbide precipitates for different regions of tempered samples: (a, b) 1/4t; (c, d) 1/2t. (d) is the high-magnification image of the white rectangle in (c).

To identify the types of carbides, the chemical composition of carbides with different sizes and morphologies was analyzed via scanning TEM combined with energy-dispersive X-ray spectroscopy (EDX) mapping and high-angle annular dark-field (HAADF) imaging. Fig. 7 presents the HAADF image of carbides of ~30–50 nm and the corresponding EDX mapping results of the 1/4t sample. The small short rod-like carbides were composed of Fe, Mn, Cr, Mo, and V. Precipitates smaller than 20 nm mainly contained Cr, Mo, and V (Fig. 7 (white arrows) and Fig. 8). A previous study revealed [18] that these rod-like carbides containing Cr, Mo, and V were $M_{23}C_6$ carbides formed in long tempered low-alloy steel. The nano-sized spherical carbides, mainly with Cr, Mo, and V, should be MC carbides. Detailed TEM analysis was conducted to investigate the crystal structure of the large carbides formed in the tempered 1/2t sample. Fig. 9(a) displays the bright-field TEM image of large needle-like carbides with a length of ~180–200 nm. Fig. 9(b) is the corresponding selected-area diffraction (SAD) pattern of the large carbide. Analysis of the SAD pattern confirmed that the large carbide was M_3C carbide with an orthorhombic

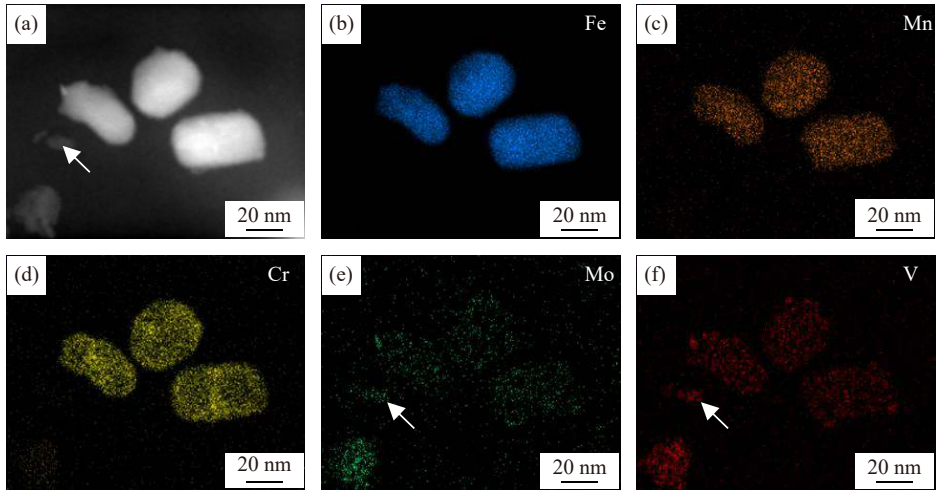

Fig. 7. TEM micrographs of the tempered 1/4t sample showing the HAADF images (a) of rod-like carbide precipitates and the corresponding elemental maps (b–f) of Fe, Mn, Cr, Mo, and V.

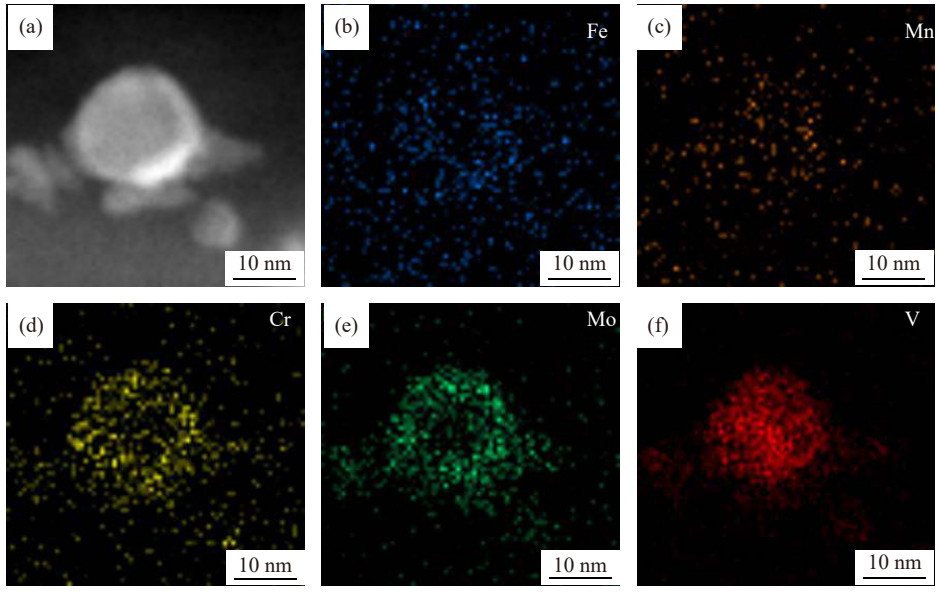

Fig. 8. TEM micrographs for the tempered 1/4t sample showing the HAADF images (a) of nanosized spherical carbide precipitates and the corresponding elemental maps (b–f) of Fe, Mn, Cr, Mo, and V.

crystal structure, and the lattice constants were ~0.45, 0.51, and 0.67 nm, respectively. These results are consistent with those of our previous study [10]. Further EDX results indicated that the M_3C carbides were composed of Fe, Cr, and Mn, and small amounts of Mo and V (Fig. 9(c–g)).

4. Discussion

4.1. Correlation between quenched microstructure and toughness

Generally, microstructural bands caused by centerline segregation are detrimental to low-temperature toughness. The mechanism underlying the deterioration has been revealed from perspectives of microstructure and the corresponding crystallographic feature. The centerline segregation region was enriched by C and Mn, resulting in abnormal high hardenability to form hard lath-like martensite [19]. The martensite transformation process at low temperatures produced high internal residual stress, which resulted in brittle fracture. Moreover, coherent phase transformation with high-level enrichment of alloying elements featured strong variant selection and produced a large packet and Bain zone size, leading to a low density of high-angle boundaries, which were unfavorable for crack deflection [20]. In the present study, the 1/4t and 1/2t regions exhibited similar toughness: ~55 J at −40°C. To elucidate the microstructure–toughness relationship, the quenched 1/4t and 1/2t regions were analyzed via EBSD. The band microstructure in Fig. 3(d) was *ex-situ* characterized via EBSD for the 1/2t region. Fig. 10(a) and (b) provides the band contrast maps and high-angle grain boundaries for the 1/4t and 1/2t regions after quenching. The white and yellow lines represent boundaries with misorientations lower and higher than 15°, respectively. The two samples exhibited similar characteristics in terms of the high density of high-angle boundaries. Fig. 10(a) and (b) shows that the density of low-angle boundaries (white lines) was a little

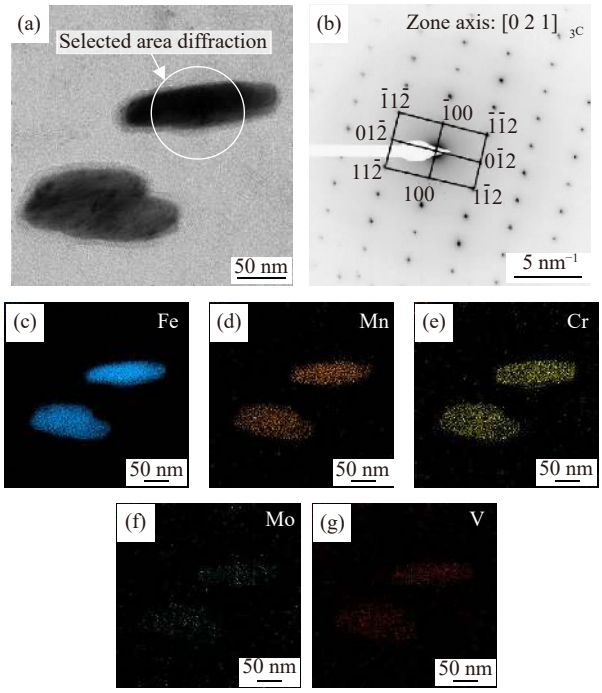

Fig. 9. Bright-field TEM image (a) and SAD patterns (b) of large carbides for the tempered 1/2t sample; (c–g) the corresponding elemental maps for Fe, Mn, Cr, Mo, and V.

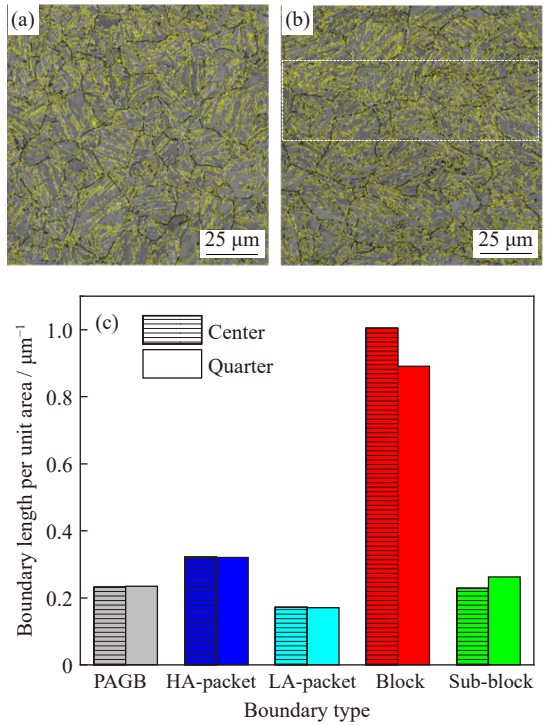

Fig. 10. EBSD results showing band contrast maps (in which the yellow lines corresponding to high-angle grain boundaries with misorientation higher than 15°) for the quenched steel plate at (a) 1/4t and (b) 1/2t regions; the white dashed rectangle region indicates the band in Fig. 2(d); (c) quantitative statistical results of different types of boundaries.

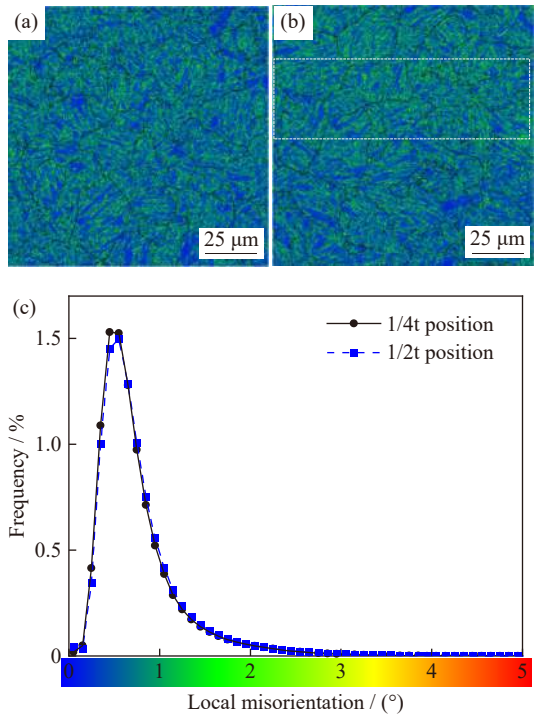

Fig. 11. EBSD results showing Kernel average misorientation (KAM) maps for the quenched steel plate at (a) 1/4t and (b) 1/2t regions, and (c) quantitative statistical results of the distribution of KAM values.

higher in the 1/4t sample, and the density of high-angle boundaries (yellow lines) was higher in the 1/2t sample. In addition, the density of high-angle boundaries was slightly higher in the banded microstructure (Fig. 10(b)). Numerous studies have indicated that prior austenite grain (PAG) [21], packet [22–23], or block/lath [24–27] are effective crystallographic units, which may influence low-temperature toughness. The densities of different types of boundaries were analyzed via machine learning [28]. The statistical results are plotted in Fig. 10(c). The densities of prior austenite grain boundaries, high-angle packet (HA-packet) boundaries, and low-angle packet (LA-packet) boundaries were almost the same between the two samples. The density of the block boundary was slightly higher in the 1/2t sample, while the density of the sub-block boundary was lower. The internal stress distribution was analyzed using Kernel average misorientation (KAM) maps (Fig. 11). The yellow and red regions represent higher stress. The stress was slightly higher in the band region (Fig. 11(b)). Through statistical analysis, only a small difference was determined at low KAM (local misorientation of ~0.5°) in the KAM distribution, and no significant difference occurred at high KAM (Fig. 11(c)). A higher KAM value means higher stress. The results indicate that no significant internal stress was introduced by the banded microstructure. Hence, the 1/4t and 1/2t samples of the quenched steel plates exhibited similar Charpy impact energy.

4.2. Effect of carbon concentration on carbide precipitation behavior

In this study, significant differences in carbide precipitation behavior occurred in the banded microstructure. Carbide precipitation largely depends on chemical composition and tempering parameters. In this study, the carbon concentra-

tion of the banded microstructure was higher than that outside the banded structures, owing to the effect of centerline segregation. Because of the difficulty in quantitatively analyzing the carbon concentration in segregated band microstructure, thermodynamic calculations on carbide precipitation at 640°C were conducted using Thermo-Calc software with the TCFE7 database for carbon concentrations of 0.05wt% to 0.30wt%. The calculated results are plotted in Fig. 12. The mole fraction of MC carbide was not significantly affected by the carbon concentration because the MC carbide was mainly (Mo, Cr, and V)C, and the mole fraction was dominated by the V content. For $M_{23}C_6$ carbide, the mole fraction increased with increasing carbon content from 0.05wt% to 0.18wt% and then decreased with a further increase in the carbon content to 0.30wt%. M_3C carbide started to form when the carbon content was 0.18wt%, and its mole fraction increased with increasing carbon content. The mole fraction reached the maximum value at a carbon content of 0.27wt% and remained constant with a further increase in the carbon content to 0.30wt%. Hence, for the studied steel with a homogeneous carbon concentration of 0.16wt%, only $M_{23}C_6$ and MC carbides could form thermodynamically. This is the thermodynamic basis for the occurrence of $M_{23}C_6$ and MC as the dominant carbides in the tempered 1/4t sample. A few M_3C carbides formed along boundaries in the 1/4t sample, attributable to carbon enrichment at boundaries during quenching. Carbon atoms preferentially segregate at the boundaries to deduce the system energy during quenching [29]. For the banded microstructure in the 1/2t sample, the carbon content should be as high to precipitate M_3C carbides. In addition, high carbon content promotes the rapid growth of $M_{23}C_6$ carbides. Therefore, large M_3C and $M_{23}C_6$ carbides were obtained in the banded microstructure after tempering.

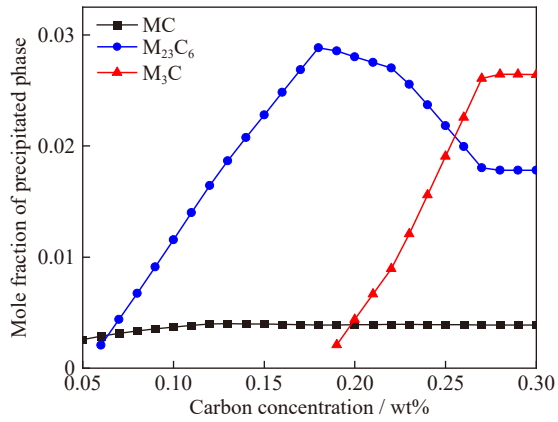

Fig. 12. Calculated mole fraction of different carbides under different carbon concentrations (obtained using Thermo-Calc software).

4.3. Correlation between carbide precipitation and toughness

To study the correlation between carbide precipitation and low-temperature toughness, the fractographs of different regions of tempered Charpy impact samples were investigated via SEM. The obtained fractographs are shown in Fig. 13. The 1/4t region of the tempered steel plate exhibited a normal quasi-cleavage fracture (Fig. 13(a) and (b)). It featured a smooth and ductile fracture with a large dimple (Fig. 13(b)). The formation of large dimples indicates a relatively high impact energy for the 1/4t region of the tempered steel plate. The obtained high strength and high toughness balance were due to the dispersed nanosized rod-like alloy carbides and MC precipitates [2,10]. However, the 1/2t sample exhibited significant delamination fracture (Fig. 13(c), white arrows). Cleavage fracture occurred in the delamination fracture region (Fig. 13(d)). In addition, large carbides containing rod-like and needle-like morphologies occurred on the smooth cleavage surface (Fig. 13(d), white arrows). One study [30] reported that carbides precipitated along grain boundaries embrittled the grain boundaries and caused delamination fracture, which ultimately reduced toughness. Therefore, the formation of a high density of large carbides in the banded microstructure is detrimental to low-temperature toughness, as the carbides induce delamination cleavage fracture. In summary, controlling centerline segregation is vital for developing 1-GPa-grade ultra-high-strength ultra-heavy steel plates, even though the manganese content is reduced to a low level. Rapid cooling during continuous casting could be beneficial for improving the internal quality of cast ingot [31]. Moreover, our previous work indicated that appropriately enhancing the superheat and reducing the current intensity of electromagnetic stirring could reduce the centerline segregation degree [32]. In addition, the tempering parameters need to be further investigated for carbide precipitation regulation, particularly in the segregated band microstructure, to obtain high strength and high toughness combination.

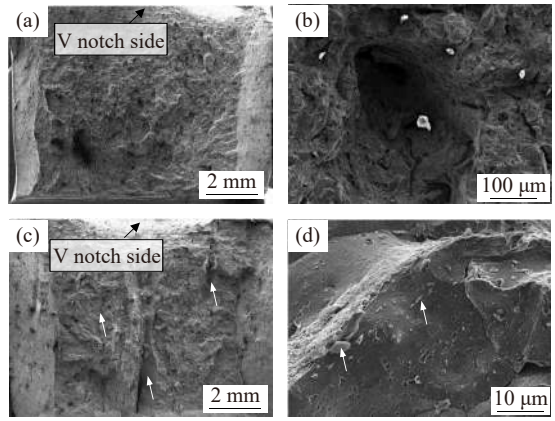

Fig. 13. SEM fractographs of Charpy impact samples of the tempered steel plate at different regions: (a, b) 1/4t region and (c, d) 1/2t region.

5. Conclusions

In this work, microstructure, carbide precipitation, and their relationships with low-temperature toughness were investigated using a 1 Gpa-grade ultra-heavy quenched and tempered steel plate. The 1/4t and 1/2t regions of the steel plate were considered, and the influence of centerline segreg-

ation was investigated. The gained conclusions are summarized below.

(1) Significant microstructure bands occurred at the 1/2t region, owing to centerline segregation. However, the 1/4t and 1/2t regions exhibited almost the same crystallographic characteristics, and no abnormal internal stress was induced by the formation of a banded microstructure, resulting in similar Charpy impact energy between both regions after quenching.

(2) The carbide precipitation behavior of the tempered steel plate was influenced by centerline segregation. For 1/4t tempered sample without segregation, the precipitates were uniformly dispersed as short rod-like $M_{23}C_6$, with a size smaller than 100 nm, and spherical MC carbides with a diameter of several nanometers to ~20 nm. The precipitates mainly occurred as large rod-like $M_{23}C_6$ and needle-like M_3C carbides. In addition, the carbide distribution in the 1/2t tempered sample was heterogeneous, and numerous coarse rod-like $M_{23}C_6$ carbides aggregated into a dense precipitate group in the segregated band region. The coarse rod-like carbides were mainly ~100–200 nm on the long axis and ~50–100 nm on the short axis. The length of the needle-like M_3C reached 1 μm. Few spherical nanosized carbides occurred in the precipitate group.

(3) The precipitation of numerous large carbides in the banded microstructure of the 1/2t region of the tempered sample was detrimental to the low-temperature toughness by inducing delamination cleavage fracture during Charpy impact. Therefore, the impact toughness for the 1/2t region was decreased by ~46% after tempering, compared with the quenched 1/2t sample.

Acknowledgements

The authors gratefully acknowledge the financial support provided by the Fundamental Research Funds for the Central Universities (Nos. FRF-TP-19-052A2 and FRF-BD-22-02), the National Natural Science Foundation of China (No. 52001023), and the Liao Ning Revitalization Talents Program (No. XLYC1907186).

Conflict of Interest

The authors declare no conflict of interest.

References

[1] Z.J. Xie, C.J. Shang, X.L. Wang, X.M. Wang, G. Han, and R.D.K. Misra, Recent progress in third-generation low alloy steels developed under M^3 microstructure control, *Int. J. Miner. Metall. Mater.*, 27(2020), No. 1, p. 1.

[2] J. Hu, L.X. Du, Y. Dong, Q.W. Meng, and R.D.K. Misra, Effect of Ti variation on microstructure evolution and mechanical properties of low carbon medium Mn heavy plate steel, *Mater. Charact.*, 152(2019), p. 21.

[3] J. Hu, L.X. Du, W. Xu, *et al*., Ensuring combination of strength, ductility and toughness in medium-manganese steel through optimization of nano-scale metastable austenite, *Mater. Charact.*, 136(2018), p. 20.

[4] X. Chen, Q.W. Cai, B.S. Xie, Y. Yun, and Z.Y. Zhou, Simulation of microstructure evolution in ultra-heavy plates rolling process based on Abaqus secondary development, *Steel Res. Int.*, 89(2018), No. 12, art. No. 1800409.

[5] S.K. Choudhary, S. Ganguly, A. Sengupta, and V. Sharma, Solidification morphology and segregation in continuously cast steel slab, *J. Mater. Process. Technol.*, 243(2017), p. 312.

[6] J. Li, Y.H. Sun, H.H. An, and P.Y. Ni, Shape of slab solidification end under non-uniform cooling and its influence on the central segregation with mechanical soft reduction, *Int. J. Miner. Metall. Mater.*, 28(2021), No. 11, p. 1788.

[7] Z.J. Xie, Q. Li, Z.P. Liu, *et al*., Enhanced ductility and toughness by tailoring heterogenous microstructure in an ultra-heavy gauge high strength steel with severe centerline segregation, *Mater. Lett.*, 323(2022), art. No. 132525.

[8] F.J. Guo, X.L. Wang, W.L. Liu, *et al*., The influence of centerline segregation on the mechanical performance and microstructure of X70 pipeline steel, *Steel Res. Int.*, 89(2018), No. 12, art. No. 1800407.

[9] A. Nagao, T. Ito, and T. Obinata, Development of YP 960 and 1100 MPa class ultra high strength steel plates with excellent toughness and high resistance to delayed fracture for construction and industrial machinery, *JFE Technol. Rep.*, 11(2008), p. 13.

[10] Z.J. Xie, Y.P. Fang, G. Han, H. Guo, R.D.K. Misra, and C.J. Shang, Structure-property relationship in a 960 MPa grade ultrahigh strength low carbon niobium–vanadium microalloyed steel: The significance of high frequency induction tempering, *Mater. Sci. Eng. A*, 618(2014), p. 112.

[11] D. Bhattacharya, G.P. Poddar, and S. Misra, Centreline defects in strips produced through thin slab casting and rolling, *Mater. Sci. Technol.*, 32(2016), No. 13, p. 1354.

[12] C.T. Zheng and Z. Chen, Carbon isoactivity curves in austenite for Fe–Mn–C alloys and Fe–Si–C alloys and their applications, *Trans. Matert. Heat Treat.*, 10(1989), No. 1, p. 79.

[13] J. Emo, P. Maugis, and A. Perlade, Austenite growth and stability in medium Mn, medium Al Fe–C–Mn–Al steels, *Comput. Mater. Sci.*, 125(2016), p. 206.

[14] M.J. Santofimia, L. Zhao, R. Petrov, C. Kwakernaak, W.G. Sloof, and J. Sietsma, Microstructural development during the quenching and partitioning process in a newly designed low-carbon steel, *Acta Mater.*, 59(2011), No. 15, p. 6059.

[15] Z.J. Xie, S.F. Yuan, W.H. Zhou, J.R. Yang, H. Guo, and C.J. Shang, Stabilization of retained austenite by the two-step intercritical heat treatment and its effect on the toughness of a low alloyed steel, *Mater. Des.*, 59(2014), p. 193.

[16] J. Pak, D.W. Suh, and H.K.D.H. Bhadeshia, Promoting the coalescence of bainite platelets, *Scripta Mater.*, 66(2012), No. 11, p. 951.

[17] K. Bhadeshia, E. Keehan, L. Karlsson, and H. Andren, Coalesced bainite, *Trans. Indian Inst. Met.*, 59(2006), No. 5, p. 689.

[18] K.H. Kuo and C.L. Jia, Crystallography of $M_{23}C_6$ and M_6C precipitated in a low alloy steel, *Acta Metall.*, 33(1985), No. 6, p. 991.

[19] L.H. Su, H.J. Li, C. Lu, *et al*., Transverse and *z*-direction CVN impact tests of X65 line pipe steels of two centerline segregation ratings, *Metall. Mater. Trans. A*, 47(2016), No. 8, p. 3919.

[20] J. Wang, F. Guo, Z. Wang, Z. Xie, C. Shang, and X. Wang, Influence of centerline segregation on the crystallographic features and mechanical properties of a high-strength low-alloy steel, *Mater. Lett.*, 267(2020), art. No. 127512.

[21] X. Li, X. Ma, S.V. Subramanian, C. Shang, and R.D.K. Misra, Influence of prior austenite grain size on martensite–austenite constituent and toughness in the heat affected zone of 700 MPa high strength linepipe steel, *Mater. Sci. Eng. A*, 616(2014), p.

141.
[22] C.F. Wang, M.Q. Wang, J. Shi, W.J. Hui, and H. Dong, Effect of microstructural refinement on the toughness of low carbon martensitic steel, *Scripta Mater.*, 58(2008), No. 6, p. 492.
[23] E. Bouyne, H.M. Flower, T.C. Lindley, and A. Pineau, Use of EBSD technique to examine microstructure and cracking in a bainitic steel, *Scripta Mater.*, 39(1998), No. 3, p. 295.
[24] C.F. Wang, M.Q. Wang, J. Shi, W.J. Hui, and H. Dong, Microstructural characterization and its effect on strength of low carbon martensitic steel, *Iron Steel*, 42(2007), No. 11, p. 57.
[25] D. Liu, M. Luo, B. Cheng, R. Cao, and J. Chen, Microstructural evolution and ductile-to-brittle transition in a low-carbon MnCrMoNiCu heavy plate steel, *Metall. Mater. Trans. A*, 49(2018), No. 10, p. 4918.
[26] S.L. Long, Y.L. Liang, Y. Jiang, Y. Liang, M. Yang, and Y.L. Yi, Effect of quenching temperature on martensite multi-level microstructures and properties of strength and toughness in 20CrNi$_2$Mo steel, *Mater. Sci. Eng. A*, 676(2016), p. 38.
[27] S. Morito, H. Yoshida, T. Maki, and X. Huang, Effect of block size on the strength of lath martensite in low carbon steels, *Mater. Sci. Eng. A*, 438-440(2006), p. 237.
[28] X.C. Li, J.X. Zhao, J.H. Cong, *et al*., Machine learning guided automatic recognition of crystal boundaries in bainitic/martensitic alloy and relationship between boundary types and ductile-to-brittle transition behavior, *J. Mater. Sci. Technol.*, 84(2021), p. 49.
[29] J.L. Wang, R. Janisch, G.K.H. Madsen, and R. Drautz, First-principles study of carbon segregation in bcc iron symmetrical tilt grain boundaries, *Acta Mater.*, 115(2016), p. 259.
[30] W. Yan, W. Sha, L. Zhu, W. Wang, Y.Y. Shan, and K. Yang, Delamination fracture related to tempering in a high-strength low-alloy steel, *Metall. Mater. Trans. A*, 41(2010), No. 1, p. 159.
[31] H.G. Zhong, R.J. Wang, Q.Y. Han, *et al*., Solidification structure and central segregation of 6Cr13Mo stainless steel under simulated continuous casting conditions, *J. Mater. Res. Technol.*, 20(2022), p. 3408.
[32] C.S. Wang, J.F. Guo, G.L. Li, and C.J. Shang, Influence of central segregation control on low temperature toughness of steel, *Iron Steel*, 54(2019), No. 8, p. 202.